Near-wall rheotaxis of the ciliate Tetrahymena induced by the kinesthetic sensing of cilia

AUTHOR(S):

Ohmura, Takuya; Nishigami, Yukinori; Taniguchi, Atsushi; Nonaka, Shigenori; Ishikawa, Takuji; Ichikawa, Masatoshi

CITATION:

Ohmura, Takuya ...[et al]. Near-wall rheotaxis of the ciliate Tetrahymena induced by the kinesthetic sensing of cilia. Science Advances 2021, 7(43): eabi5878.

ISSUE DATE:

2021-10

URL:

http://hdl.handle.net/2433/265517

BIOPHYSICS

Near-wall rheotaxis of the ciliate *Tetrahymena* induced by the kinesthetic sensing of cilia

Takuya Ohmura[1,2*†], Yukinori Nishigami[3,4*†], Atsushi Taniguchi[5,6], Shigenori Nonaka[5,6], Takuji Ishikawa[7,8], Masatoshi Ichikawa[9*]

To survive in harsh environments, single-celled microorganisms autonomously respond to external stimuli, such as light, heat, and flow. Here, we elucidate the flow response of *Tetrahymena,* a well-known single-celled freshwater microorganism. *Tetrahymena* moves upstream against an external flow via a behavior called rheotaxis. While micrometer-sized particles are swept away downstream in a viscous flow, what dynamics underlie the rheotaxis of the ciliate? Our experiments reveal that *Tetrahymena* slides along walls during upstream movement, which indicates that the cells receive rotational torque from shear flow to control cell orientation. To evaluate the effects of the shear torque and propelling speed, we perform a numerical simulation with a hydrodynamic model swimmer adopting cilia dynamics in a shear flow. The swimmer orientations converge to an upstream alignment, and the swimmer slides upstream along a boundary wall. The results suggest that *Tetrahymena* automatically responds to shear flow by performing rheotaxis using cilia-stalling mechanics.

INTRODUCTION

Microorganisms play an essential role in ecosystems and are crucial to the food chain of living beings on Earth. Recently, the classification system of eukaryotes has been organized on the basis of genetic information, and it has become clear that the diversity of eukaryotes is borne by protists. It has also become clear that the diversity of protists plays an important role in maintaining the global environment. Organisms including protists generally respond to stimuli from the external environment in an appropriate manner to survive in nature. This type of behavior, especially translational motion, is termed taxis. For instance, organisms move closer to chemicals that are beneficial to them and farther from chemicals that are detrimental to them, which is called chemotaxis. Light, temperature, electric and magnetic fields, etc., are well known as targets of taxis in various living organisms. Here, we focus on protists' behavior toward fluid flow, so-called rheotaxis, which is essential for the survival of single-celled swimming organisms in fresh water.

One class of protists, ciliates, is a major organism of inland water and supports water ecosystems. In general, swimming ciliates have hundreds of hair-like organelles, termed cilia, that beat around the whole body to induce swimming thrust force. To feed on sedimented nutrients, ciliates frequently accumulate on solid-fluid interfaces, such as the bottom of lakes and the surface of water weeds (*1*–*6*). In nature, ciliates always face a serious risk of being swept away from the surfaces by an external flow. Therefore, ciliates require a function or a strategy to resist flow perturbations.

Rheotaxis is well known as a common property of freshwater fish to swim against currents, which generally sweep toward seawater, where the fish cannot live (*7*–*10*). Although some swimming cells do not have organelles to sense fluid flow, they exhibit rheotaxis (*7*). In a viscous fluid, intuitively, it seems impossible for swimmers to achieve a faster flow than their swimming speeds. Successful key factors for the rheotaxis of swimming cells have been revealed in a physical swimming model (*11*–*18*). This model categorizes swimming styles into three patterns: pusher, puller, and neutral swimming. A pusher swims driven by rear flagella. The rheotaxis of pushers in a shear flow close to a wall has been reported in, for instance, mammalian sperm (*11*, *13*, *19*, *20*) and bacteria (*12*, *15*, *16*). Those studies show that a contact interaction between an elongated cell shape and a wall induces pusher rheotaxis. A puller swims driven by anterior flagella (e.g., *Chlamydomonas* and *Euglena*). In a theoretical study, pullers were found to swim upstream under a background flow with only a hydrodynamic interaction with a wall (*21*). However, numerical models of the neutral swimmer, which swims using cilia or multiple flagella around a body (e.g., ciliates and *Volvox*), cannot accommodate swimming against a flow even close to a wall.

Then, how does the rheotaxis of actual ciliates occur? In 1906, it was reported that *Paramecium*, a kind of ciliate, exhibits rheotaxis (*22*), which is opposite to the present theoretical model. However, since that report, no research has been conducted on the rheotaxis of ciliates, which indicates that neither detailed observations nor the physical mechanism of ciliate rheotaxis has been pursued.

Here, we investigated the response of a ciliate, *Tetrahymena pyriformis*, to shear flow near a wall. Detailed observations and fluid simulations suggest previously unidentified mechanisms of ciliate rheotaxis from the kinesthetic sensing system of cilia.

RESULTS

The ciliate *Tetrahymena* showed positive rheotaxis close to a wall

To observe the behavior of *T. pyriformis* in water flow, we placed cells into a rectangular microchannel and applied flow controlled by a pressure pump (Fig. 1A). The generated flow exhibited a Hele-Shaw

[1]Max Planck Institute for Terrestrial Microbiology, Marburg 35043, Germany. [2]Biozentrum, University of Basel, Basel 4056, Switzerland. [3]Research Center of Mathematics for Social Creativity, Research Institute for Electronic Science, Hokkaido University, Sapporo 001-0020, Japan. [4]Global Station for Soft Matter, Global Institution for Collaborative Research and Education, Hokkaido University, Sapporo 001-0021, Japan. [5]Laboratory for Spatiotemporal Regulations, National Institute for Basic Biology, Okazaki 444-8585, Japan. [6]Spatiotemporal Regulations Group, Exploratory Research Center on Life and Living Systems (ExCELLS), Okazaki, Aichi 444-8585, Japan. [7]Graduate School of Engineering, Tohoku University, Aoba, Sendai 980-8579, Japan. [8]Graduate School of Biomedical Engineering, Tohoku University, Aoba, Sendai 980-8579, Japan. [9]Department of Physics, Kyoto University, Sakyo, Kyoto 606-8502, Japan.
*Corresponding author. Email: takuya.ohmura@unibas.ch (T.O.); nishigami@es.hokudai.ac.jp (Y.N.); ichi@scphys.kyoto-u.ac.jp (M.I.)
†These authors contributed equally to this work.

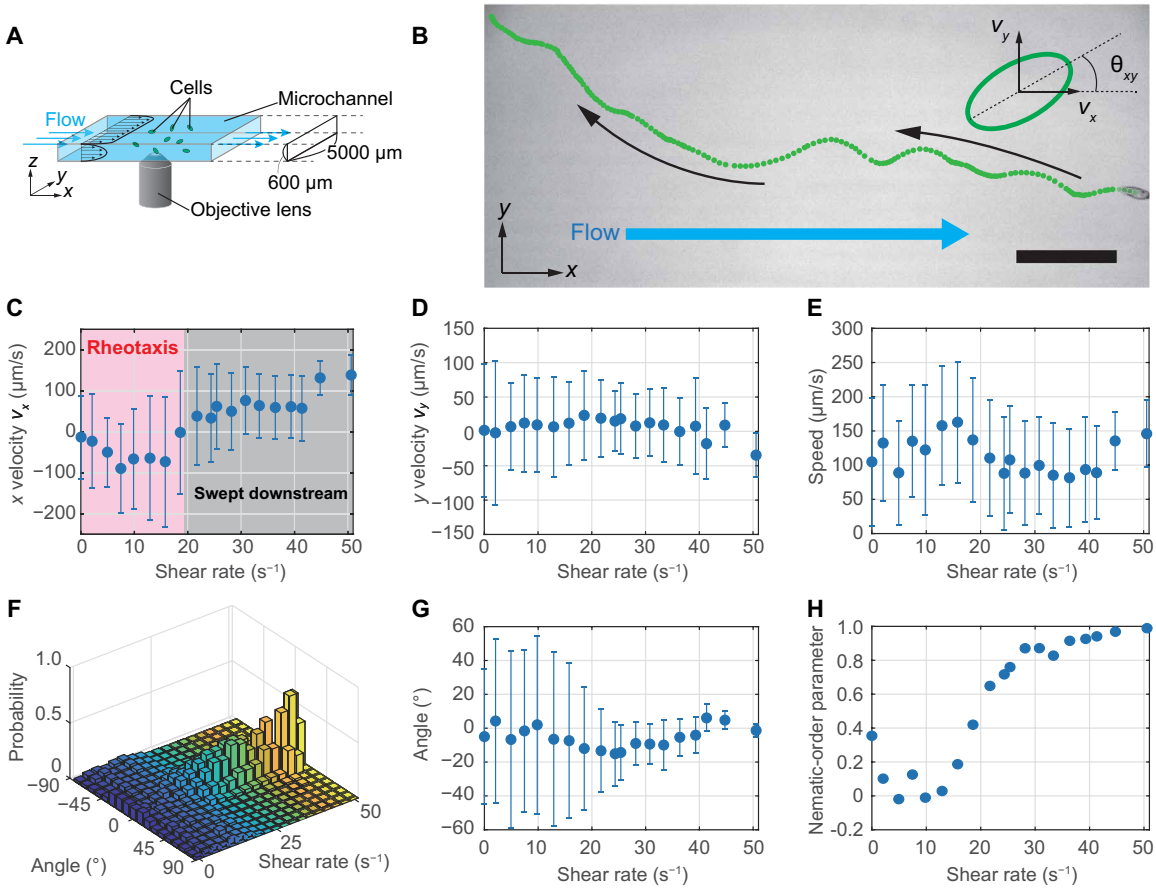

Fig. 1. Motility and orientation of *T. pyriformis* under shear flow. (**A**) Experimental setup for the observation of cells in a rectangular microfluidic channel. We observed cells on the *xy* bottom wall of the channel by microscopy. The cells experienced shear flow, which was assumed to involve linear shear close to the bottom wall. (**B**) A typical trajectory of a rheotaxic cell. The cell slid against the flow on the bottom wall. The top blue vector represents the flow direction. The black vectors represent the moving directions of the cell. The time interval of each position is 30 ms. Scale bar, 200 μm. The inset figure presents a schematic picture of the measured parameters. (**C**) Plot of the *x* velocity v_x as a function of the shear rate. Plots in the red area represent positive rheotaxis. When the shear rate was higher than a characteristic rheotaxic shear rate 19.4 s^{-1} (gray area), the cells showed negative rheotaxis or were swept away downstream. (**D**) Plot of the *y* velocity v_y as a function of the shear rate. (**E**) Plot of the speed as a function of the shear rate. (**F**) 3D histogram of θ_{xy}, the angle of the long axis on an ellipse-fitted cell. With increasing shear rate, θ_{xy} converged. (**G**) Plot of θ_{xy} as a function of the shear rate. (**H**) 2D nematic-order parameter between θ_{xy} and the flow direction. The value quickly increased around the characteristic rheotaxic shear rate. Error bars represent the SD.

flow profile in the center of the channel along the *y* axis and was parabolic along the *z* axis. In particular, near the top and bottom walls of the channel, the flow field can be approximately regarded as a shear flow along the *z* axis. When the cells were swimming far from the wall, they flowed downstream. On the other hand, the cells on the bottom wall moved upstream adjacent to the wall under shear flow (Fig. 1B and movie S1). Since the inside surface of the channel was coated by 2-methacryloyloxyethyl phosphorylcholine (MPC) polymer to prevent cell wall adhesion, the cells did not adhere to the wall, but they retained freedom for translational sliding on the wall. The analyzed data were obtained only from the in-focus cells on the wall, while cells far from the wall were excluded. Figure 1C shows the *x* velocities of the cells. When the shear rate was 2.1 $s^{-1} < \dot{\gamma} <$ 18.6 s^{-1}, the mean *x* velocity was negative, which indicates that the cells swam against the flow, corresponding to positive rheotaxis. The *x* velocity decreased to its peak value at $\dot{\gamma}$ = 7.5 s^{-1} and then increased. When $\dot{\gamma}$ > 21.7 s^{-1}, the cell mean velocity and the cell population following the translational motion direction showed that the cells underwent a change from positive to negative rheotaxis (movie S2). Here, negative rheotaxis indicates cells moving downstream along the wall. By counting the number of cells showing positive rheotaxis ($v_x < 0$), we estimated a characteristic rheotaxic shear rate to determine whether the cells expressed positive rheotaxis or not, $\dot{\gamma}_c$ = 19.4 s^{-1} (fig. S1). Note that the cells with near-zero speeds corresponding to slowly sliding cells resisting the flow were conspicuous for a long time in the observation window, even at the above $\dot{\gamma}_c$. In long-term observations, few cells incidentally landed on the wall with an arbitrary direction and kept their direction during the observation time window at higher shear rates. Although the ensembles include the abovementioned cases, approximately half of the cells at the above $\dot{\gamma}_c$ were drifting downstream, and most cells at the above $2\dot{\gamma}_c$ were swept downstream. The absolute values of the *y* velocities were less than those of the *x* velocities, which means that the cells did not move exactly parallel to the *x* axis and presented a certain angle between the moving direction and the *x* axis (Fig. 1D). The speeds of cells moving along the wall reached 162.8 μm/s (Fig. 1E).

To confirm the translational motions and directors of the cells, we also measured the *xy* angle θ_{xy} of the cell orientation by fitting cells with ellipses (Fig. 1B, inset). The flow direction was identical to $\theta_{xy} = 0$. In addition, θ_{xy} was distributed homogenously at $\dot{\gamma} = 0\ s^{-1}$, and the distribution of θ_{xy} gradually converged as the shear rate increased (Fig. 1F). The averaged θ_{xy} at each shear had a peak value of $-15.1°$ at $\dot{\gamma} = 24.3\ s^{-1}$ and then returned to 0° (Fig. 1G). The negative peak of θ_{xy} was related to the abovementioned *y* velocity. We discuss the reason below. Figure 1H shows a two-dimensional (2D) nematic-order parameter of θ_{xy} as a function of the shear rate. The nematic-order parameter *S* in 2D space is defined as $S \leq 2\cos^2(\theta_{xy} - \theta_{flow}) - 1>$, where <> denotes an ensemble average and θ_{flow} is the flow direction. $S = 1$ means that all cell orientations are completely aligned with the flow direction. At a small shear rate below the characteristic shear rate $\dot{\gamma}_c = 19.4\ s^{-1}$, *S* was close to zero. However, above $\dot{\gamma}_c$, *S* markedly increased to nearly one, which indicates that the alignment of the cell orientation changed in the manner of a phase transition. This tendency also exhibited a decay of the SD of θ_{xy} (fig. S2).

Kinesthetic sensing of cilia: The ciliary beating of the ciliate sliding upstream was asymmetric

The behavior against the flow is expected to be induced by the swimming apparatus, i.e., cilia, because there is not much to compete with the shear flow but an active propelling force generated by this swimming apparatus and its distribution. We checked the ciliary beating of a cell sliding upstream using a transverse microscope with light sheet illumination. When *T. pyriformis* collides with a solid wall without a shear flow, it slides along the wall due to a ciliary stop near the wall (*5*), while a model swimmer without the cilia response is repelled from the wall in simulations and in the analytical solution. We visualized ciliary beating of a cell moving upstream in a capillary flow (Fig. 2A). Note that the cells experienced a Hagen-Poiseuille flow in this thin tube, and the cells on the capillary wall could be approximately considered to be located in a linear shear flow and in the rectangular microfluidic channel (Fig. 2, B and C). Figure 2D shows snapshots of the cell moving and exhibiting positive rheotaxis under shear flow $\dot{\gamma} = 5.0\ s^{-1}$. While the ciliary beating on the upper side was not attached to the wall and occurred dynamically, the ciliary beating on the bottom side was stalled. Therefore, when the cells showed positive rheotaxis, the motility of ciliary beating became asymmetric between the bottom and top sides.

The above experimental results for the sliding behavior along the wall are consistent with previous works on ciliate sliding along a wall without flow, which suggests that the positive rheotaxis of the ciliates did not come from cell wall adhesion but from the wall-sliding behavior. In addition, the thrust force from ciliary beating around the body was asymmetrical, which means that the cells experienced torque driving them to stay on the wall (fig. S3), even under shear flow. In the next simulation part, we estimate the contribution of ciliary thrust force asymmetry to reveal the mechanism of rheotaxis.

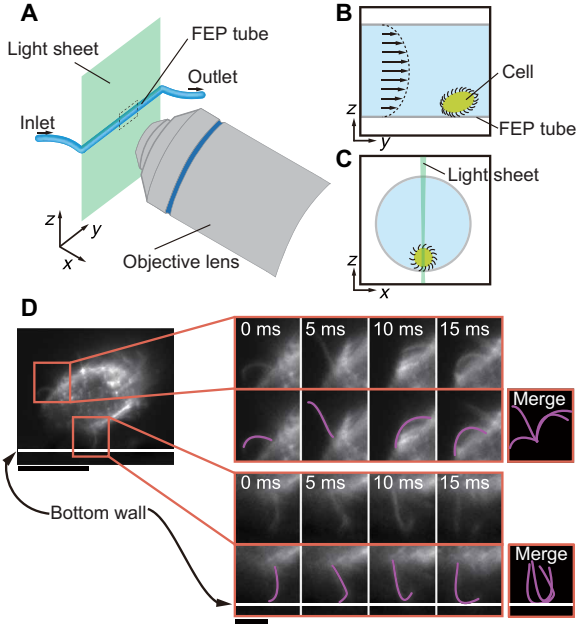

Fig. 2. Asymmetric ciliary beatings around a sliding cell under shear flow. (**A**) Experimental setup for fluorescent observation with light sheet microscopy. Cells were placed in a fluorinated ethylene polypropylene (FEP) tube and allowed to flow. (**B**) A schematic figure of the cells inside the tube (side view). In the tube, the cells experienced a Hagen-Poiseuille flow and slid upstream adjacent to the inner wall. (**C**) A schematic figure of the cells inside the tube (front view). The light sheet was aligned along the tube, and the sliding cells were scanned through the FEP tube. (**D**) Snapshots of ciliary beating around a sliding cell. Left: The sliding cell on the bottom wall. Scale bar, 40 μm. We traced the cilia in the pictures using pink lines. Top: Cilia that were not attached to the wall were actively beating and when the cell swam in bulk water. Bottom: The attached cilia were inactive. Snapshots were taken at 5-ms intervals. Scale bar, 10 μm.

The mathematical ciliate model with the kinesthetic sensing of cilia showed positive rheotaxis

Hydrodynamic numerical calculations with a mathematical model for ciliates that uses the boundary element method are applied to the wall and shear flow conditions. A body surface of a numerical swimmer is defined as a solid ellipsoid and is split into small elements. Assuming that the thrust force generated by cilia is uniformly distributed on the body and acts in the tangential direction, a uniform tangential force distribution is introduced slightly above the body surface (Fig. 3A). The numerical swimmer is located close to the nonslip solid wall (Fig. 3B). To reproduce the asymmetricity of ciliary beating, a "stop beating area" (SBA) is defined on the wall. The asymmetricity provides a rotational torque toward the wall to a numerical swimmer. The SBA is an essential condition for swimmers to stay on a wall, and they must detach from the wall without the SBA because of a hydrodynamic repulsion force (*5*). The SBA range is fixed to the optimized value $a = 0.3$ for *T. pyriformis* (*5*, *6*). The parameters in this simulation are shown in Fig. 3C. The boundary condition does not include lateral friction here or in the experiments. The relationships of the parameters between the experiments and the simulations are shown in table S1. The details of the numerical setup are presented in Materials and Methods.

First, we investigated a numerical swimmer under an external shear flow in the *xz* plane. Figure 4 (A to E) and fig. S4 show snapshots and trajectories of the swimmers under shear flow $\dot{\gamma}_* = 0.5$ in the positive *x* direction. The presence of the SBA and the shape of the swimmer were compared. The spherical swimmer represents the typical mathematically idealized swimmer, while the ellipsoidal swimmer imitates the actual cell shape. All the swimmers started to swim at $(x, y, z) = (0,0,0)$ toward the nonslip boundary wall at $z = -2$. To slide upstream along the boundary, the swimmer must move toward the negative *x* axis, and the swimming angle must be

$90° < \theta_{xz} < 180°$. Without the SBA, both the spherical swimmer and ellipsoidal swimmer moved away from a wall and flowed with a tumbling motion by the shear flow (Fig. 4, A and B, and movie S5). After the swimmers attached to the nonslip boundary wall, they were conveyed downstream, and their swimming directions θ_{xz} were rotated continuously by the shear flow (Fig. 4F). In the case of the spherical swimmer with the SBA and in the cases of that without the SBA, the swimmer was detached and flowed downstream (Fig. 4C). The swimmer stayed on the boundary, and the swimming direction was $\theta_{xz} < 180°$ at approximately 4000 steps (= 3.53 s) (Fig. 4F), but, lastly, the swimmer detached and rotated far from the wall. In contrast, the ellipsoidal swimmer with the SBA slid upstream along the boundary (Fig. 4D and movie S4). After colliding with the wall, the body angle smoothly converged, and the swimmer kept sliding upstream stably, as did the swimming cell in the experiments.

We checked the dependence of the sliding motion on the shear rate with the SBA. With increasing $\dot{\gamma}_*$, the ellipsoidal swimmer stayed on the wall when $\dot{\gamma}_* < 1.5$ and detached from the wall when $\dot{\gamma}_* = 1.75$ (fig. S5C), and the spherical swimmer stayed on the wall when $\dot{\gamma}_* < 0.45$ and detached from the wall when $\dot{\gamma}_* = 0.5$ (fig. S5D). The ellipsoidal swimmer showed positive rheotaxis ($v_x < 0$) when $0.5 \leq \dot{\gamma}_* \leq 1.0$ and negative rheotaxis ($v_x > 0$) when $\dot{\gamma}_* = 0.25, 1.25$, and 1.5 (fig. S5A). At $\dot{\gamma}_* = 0.25$, the swimmer was directed to the flow because the shear was too weak, and the swimmer attached to the wall could not turn on the *xz* plane (fig. S5E). We discuss the weak shear flow in the following. The spherical swimmer did not show positive

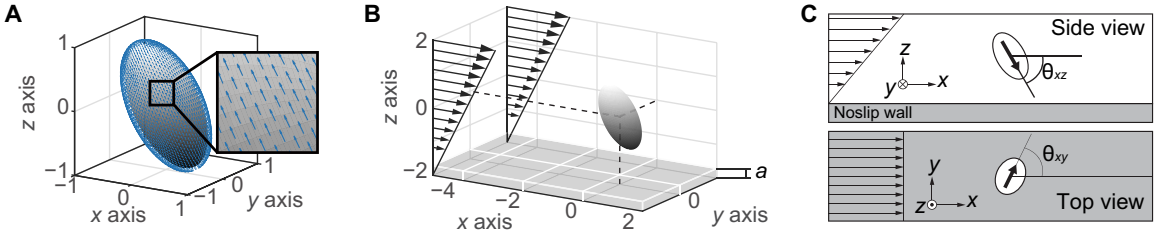

Fig. 3. Model of ciliates swimming in a shear flow close to a nonslip boundary. (**A**) A 3D numerical swimmer of a mathematical model of ciliates is defined as a rigid ellipsoid (a gray object). Its surface is discretized into triangular elements for the boundary element method. Each node in an element has a thrust point force slightly far from the rigid surface (blue vectors). (**B**) A 3D schematic of the numerical system. The swimmer is located in a linear shear flow close to a nonslip wall. Black vectors represent the shear flow. (**C**) Parameter setup. An ellipsoid represents a swimmer, and the black vectors show the swimming direction. Top: A schematic on the *xz* plane, where θ_{xz} is the angle between the longitudinal axis of the swimmer and the wall. Bottom: A schematic on the *xy* plane, where θ_{xy} is the angle between the longitudinal axis and the flow direction.

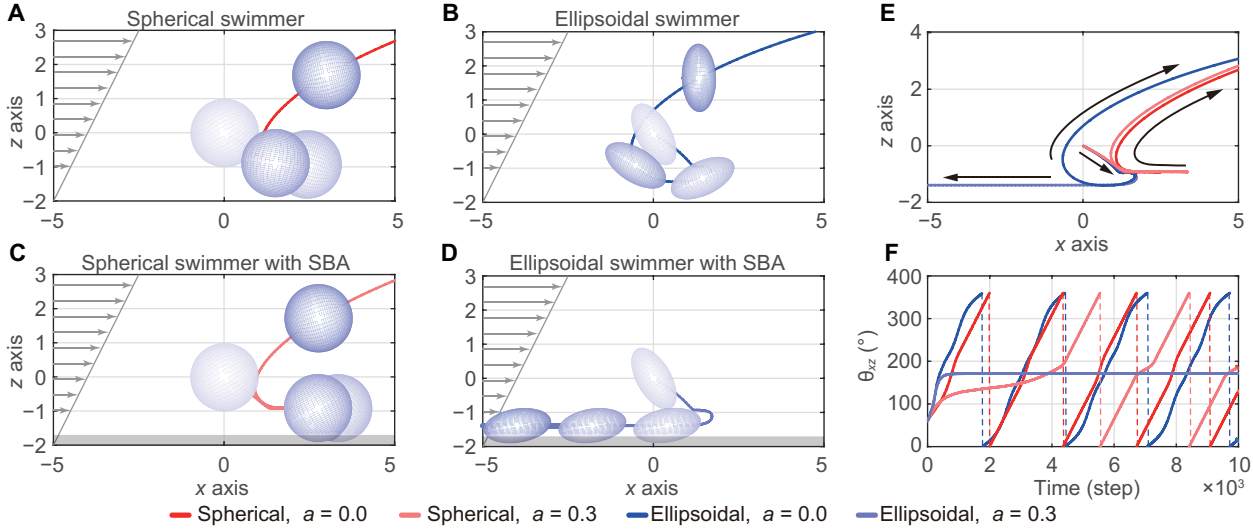

Fig. 4. Spherical and ellipsoidal swimmers with and without SBA in a shear flow. (**A** to **D**) Snapshots of trajectories in the *xz* plane of numerical swimmers under shear flow under four conditions. The color depth of objects in the plots becomes darker over time (from pale blue to deep blue). The flow direction points to the right. The shear rate $\dot{\gamma}_* = 0.5$, the initial angle $\theta_i = 60.0°$, and the initial position $(x, y, z) = (0,0,0)$ are the same in all cases. (A and B) A spherical swimmer and an ellipsoidal swimmer without the SBA. Both swimmers attached to the wall once, but they could not stay on the wall. (C) A spherical swimmer with the SBA. The swimmer stayed on the wall for a few moments but was eventually swept away. (D) An ellipsoidal swimmer with the SBA. After attaching to a wall, the swimmer started sliding in the direction opposite to the flow. (**E**) Trajectories of the four swimmers in (A) to (D). The black vectors indicate the directions of the trajectories. Only the ellipsoidal swimmer with the SBA made upstream progress. (**F**) Time evolutions of θ_{xz}. All swimmers started with motion in the bottom-right direction. The spherical and ellipsoidal swimmers without the SBA (dark red and dark blue) continuously rotated, which indicates that they were swept by the shear flow. A step in the simulation represents 0.0881 s in real time. The spherical swimmer with the SBA (light red) gradually changed its θ_{xz} until 4000 steps (= 3.53 s) and then started rotating. In the case of the ellipsoidal swimmer with the SBA, θ_{xz} converged to 171.1°.

rheotactic motions at any shear rate (fig. S5B). Even if the swimming direction was against the flow, the swimmer was carried in the flow direction by the drag force.

xy alignment of the mathematical model

We examined the dependence of the motility on the initial *xy* angle θ_i (Fig. 5, A and B, and movie S6). The ellipsoidal swimmers did not detach for any θ_i (Fig. 5A, top) and lastly slid upstream with their orientations parallel to the *x* axis [Fig. 5, A (bottom) and B]. Figure S7 indicates the motions of the spherical swimmer with changing θ_i. For any θ_i, the spherical swimmers were also directed parallel to the flow and attached to the wall; however, they moved downstream only (fig. S7). Unexpectedly, without additional conditions, the numerical swimmers aligned their orientation along the flow direction in the *xy* plane. This alignment did not depend on the shape of the swimmer. Thus, our model reproduced the experimental results in the *xz* and *xy* planes, indicating that the mechanism underlying ciliate rheotaxis can be simplified as a physical problem in 3D space.

DISCUSSION

Comparison of parameters between the actual ciliate and the mathematical model

We quantitatively compared the simulation with the experimental results. Figure 5C shows the converged *x* velocities of the numerical swimmers sliding on the wall, where the shear rate was converted to the experimental unit. Although the swimming directions of the numerical swimmers converged to alignment along the *x* axis, those in the experiments were still random at a low shear rate. The average *x* velocity diminished at the low shear rate due to the randomness in motion, while the individual propelling speeds of the cells were not notably changed from those of normally sliding cells. Thus, the average value at the low shear rate is not directly comparable between the experiments and the simulations. However, when the actual cells were aligned with the negative *x* direction at $\dot{\gamma} > 7.5\ s^{-1}$, both *x* velocities increased to 0 and increased as the shear rate increased. In addition, we studied a range of shear rates. The ellipsoidal swimmer could stay on the wall when $\dot{\gamma} < 17.0\ s^{-1}$. The swimmer detached from the wall when $\dot{\gamma} > 19.8\ s^{-1}$. This value is close to $\dot{\gamma}_c = 19.4\ s^{-1}$. Thus, the range of the shear rate where the swimmers could show rheotaxis was almost identical between the experiments and the simulations. On the other hand, the converged *x* velocity of the spherical swimmer was not proportional to the shear rate, which indicates that spherical-shaped swimmers are less amenable to rheotaxis than ellipsoidal-shaped swimmers (Fig. 5C). This result indicates that the ellipsoidal shape of the actual cell contributes to avoiding being carried downstream.

Dynamics of positive rheotaxis in the *xz* plane

We discuss how the swimmers can stay on a wall. If there is no shear flow, then a swimmer is assumed to move along the wall with the SBA. First, in the case that a swimmer drifts downstream along the wall, the swimmer is rotated by the shear flow and is directed upstream. Then, it is unclear whether the swimmer can continue to move along the wall. The swimmer experiences two torques: One is a nose-down torque from the asymmetricity of ciliary beating T_b, and the other is a nose-up torque from a shear flow T_s (Fig. 6A). If T_s is higher than T_b, then the head of the swimmer is directed up toward the wall, and it flows away. If T_s is lower than T_b, then the head of the swimmer is directed down toward the wall, and it can slide upstream along the wall.

Dynamics of cell alignment in the *xy*-plane

The next discussion is about the change in cell orientation toward the upstream direction in the *xy* plane. For any initial *xy* angle, the orientation of a swimmer finally becomes parallel to the *x* axis (Fig. 5A and figs. S6 and S7). In addition, even if the shear rate is lower ($\dot{\gamma} = 0.25$), an ellipsoidal swimmer could rotate and turn toward the upstream direction along the wall in the *xy* plane (fig. S6). It is nontrivial how the swimmer turns in the *xy* plane by considering only the flow because the flow profile has only an *x* component and a shear component does not exist in the *xy* plane. This turning motion of the swimmer can be explained by the cell shape, such as Jeffery's orbits for an ellipsoid under shear flow (*11*, *12*, *15*, *23*). Assuming that the cell body is spatially fixed by one pole of the ellipsoidal axis with a constant elevation angle, the authors identified an

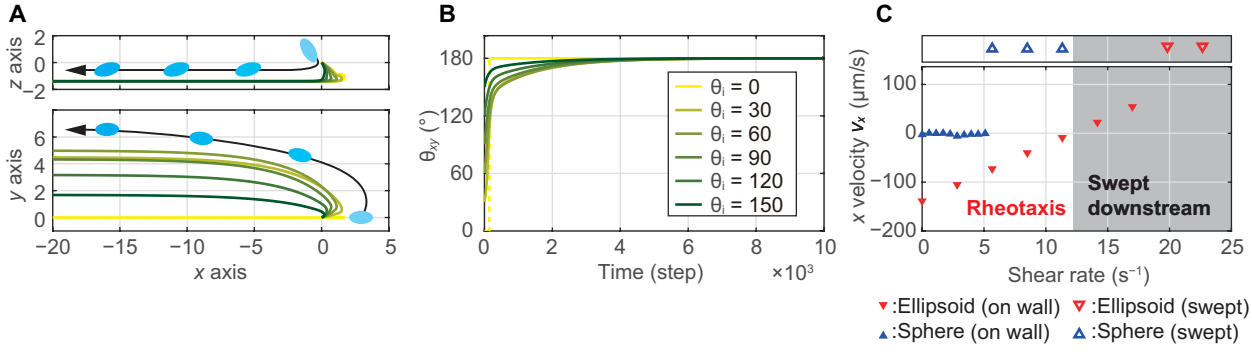

Fig. 5. Evaluation of rheotaxis of numerical swimmers. (**A**) Dependence of the initial *xy* angle θ_i. Top: Trajectories on the *xz* plane. None of the swimmers detached from the wall. Bottom: Trajectories on the *xy* plane. In all cases, the swimmers lastly slid against a flow parallel to the *x* axis. (**B**) Time evolutions of the *xy* angle. In all cases, θ_{xy} converged to 180°. The color depth in the plots denotes the change in θ_i. In all cases, $\gamma_* = 0.5$ and the initial $\theta_{xz} = 60.0°$ were fixed. (**C**) The *x* velocities of the swimmers with the shear rate. The *x* velocity of the ellipsoidal swimmers with the SBA linearly decreased until $\dot{\gamma} = 17.0\ s^{-1}$ (filled red triangles). Above $\dot{\gamma}_c = 19.8\ s^{-1}$, the ellipsoidal swimmers were swept in the flow; therefore, the velocities were large and positive (empty red triangles). The spherical swimmer stayed on the wall until $\dot{\gamma} = 5.1\ s^{-1}$ (filled blue triangles) and detached at $\dot{\gamma} = 5.7\ s^{-1}$ (empty blue triangles). The gray area in the plot represents the shear rate at which the ellipsoidal swimmer was swept downstream including the case with sustaining the slide motion as defined in the experiments.

azimuth torque to align the body toward the upstream direction when the ellipsoid had a given elevation angle of (*11*) $T_{s(azimuth)} \propto \frac{\partial \theta_{xy}}{\partial t} = -\dot{\gamma} a \sin\theta_{xy}$, where a includes the elevation angle of the cell body and the anterior point is fixed in space (see the Supplementary Materials). This force presents azimuthal orientation for the xy plane, a stable fixed point at $\theta_{xy} = 180°$ against the upstream flow and an unstable fixed point at $\theta_{xy} = 0°$. The required elevation angle is provided by the balance between T_b and T_s (Fig. 6A). A swimmer with a finite elevation/inclination angle relative to the flow direction rotates by a shear flow [$T_{s(azimuth)}$], and the rear of the swimmer approaches the wall ($T_{elevation}$) (Fig. 6B). The rear of the swimmer rises because of T_b (Fig. 6B). Although spinning torque along the major axis of the cell body is not considered here due to body symmetry, the above factors concurrently act on the swimming direction aligned upstream in the xy plane. We briefly note an additional difference in xy trajectories between the experiment and simulation. The numerical swimmers eventually traveled upstream along the x axis, whereas the cells in the experiments moved not quite parallel to the x axis but rather diagonally and had positive y velocities under shear flow (Fig. 1, C and D, and movie S1). The tilt of the azimuth angle arose from the cell shape and the thrust force of the cilia (*5*, *24*, *25*). On the wall, the cells sliding with circular clockwise trajectories from the bottom view (plus rotation for the z axis, right-hand rule) started to move in the direction mentioned above under shear flow. Therefore, alignment with the upstream direction can be understood in terms of two aspects considering the discussion mentioned above, where the ensemble directions converge in the chirality-determined direction upstream under a moderate shear rate and where the ensemble or nematic directions align upstream under moderate and higher shear in parallel (Fig. 1H). Although the contributions of the shape and the thrust force have not been identified here, the experimentally yielded chiral parameter, now named the Ishimoto constant (*24*), can be calculated as $\alpha \sim 0.06\beta$, where β is the Bretherton constant, and $\theta_{xz} \sim 170°$ and $\theta_{xy} \sim -10°$ are used. Regarding the alignment dynamics, the value of the active propelling speed (U) normalized by the body size (L) indicates the shear strength at the beginning of the isotropic-nematic transition ($\dot{\gamma} \sim 10.0\ s^{-1}$ and $U/L \sim 10\ s^{-1}$), as shown in Fig. 1H and fig. S8. This is intuitively reasonable considering the competition between the self-rotating (antialigning) motion and the speed (U) and flow speed near the wall ($\dot{\gamma}L$) for rheotaxis (*20*), but a detailed mechanism with theoretical considerations has yet to be presented.

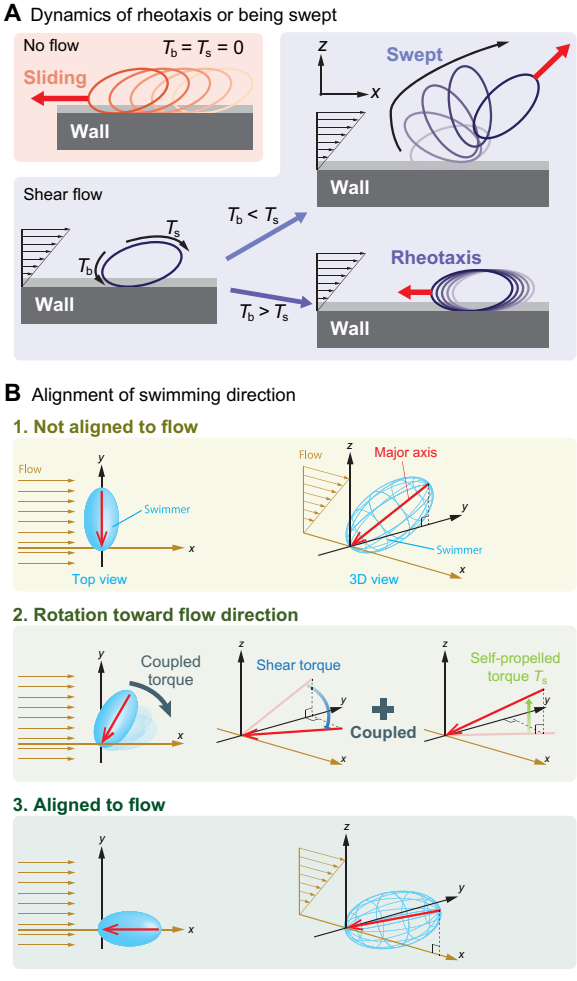

Fig. 6. Schematic figures of the dynamics of rheotaxis and alignment. (**A**) The green and blue ellipsoids represent the swimmer, and the light gray area represents the SBA. T_b is the torque arising from the asymmetricity of the thrust force. T_s is the combined torque from a shear flow and the hydrodynamic interaction with a wall. As shown in the top-right and bottom-right figures, the swimmer detached at $T_b < T_s$, and the swimmer could stay on the wall at $T_b > T_s$. (**B**) The swimmer's orientation θ_{xy} automatically becomes aligned with the flow direction when the swimmer slides along a wall due to a coupling of the shear torque and self-propelled torque.

In summary, swimmers on a wall with thrust force stalling showed rheotaxis until reaching $\dot{\gamma}_c$, regardless of the incident angle. We determined that *T. pyriformis* showed positive rheotaxis and aligned along a flow direction in a microchannel. The cells could stay on a wall without cell adhesion and slid upstream under shear flow. The hydrodynamic numerical simulations that induce the physical essential factors of rheotaxis are the asymmetry of ciliary motility and the ellipsoidal shape of the cell body. While ciliates do not have organelles to sense flow, they can "sense" flow direction and move exactly upstream for efficient survival due to the kinesthetic sensing of cilia to stay close to a solid surface. In conclusion, the rheotaxis of ciliates can be described through simpler dynamics than biochemical mechanisms. We expect that these findings can be applied to the dynamics of other organisms or other taxis systems.

MATERIALS AND METHODS

Preparation of *T. pyriformis*

T. pyriformis was donated by O. Numata (University of Tsukuba, Japan). The cells were cultured in growth medium [1.2% (w/v) Bacto Proteose Peptone (Becton, Dickinson and Company), 0.6% (w/v) Paticase (Kyokuto), and 0.2% (w/v) Bacto Yeast Extract, (Becton, Dickinson and Company)] at room temperature (20° to 25 ° C) with aeration (e-AIR6000WB, GEX). Serial transfer of the cells was performed twice per week. Before observation, the cells in midlog phase were washed three times with observation solution [10 mM Mops/tris (pH 7.2), 1 mM KCl, 1 mM NaCl, and 1 mM $CaCl_2$] (*26*) and equilibrated with observation solution for more than 1 hour before observation.

The shape of the cells used in the experiments was approximated as an ellipse, where the mean major length was 52.3 μm and the mean minor length was 24.8 μm. The mean swimming speed far from a wall without external flow was 281.4 μm/s.

Observation of the behavior of *T. pyriformis* in a microfluidic channel

To observe the response of *T. pyriformis* to flow and shear, we used the microfluidic setup depicted in Fig. 1A. While applying pressure onto the observation solution in a microchannel, the cells in the microchannel were observed by microscopy. The length (x axis) of the microchannel (produced from ibidi μ-Slide I Luer, no coating) was 50 mm, the width (y axis) was 5000 μm, and the height (z axis) was 600 μm. The inside surface of the microchannel was coated with MPC polymer (Lipidure-CM5206, NOF CORPORATION) to prevent cell adhesion to the substrate. The flow in the channel was controlled by a microfluidic pump with a pressure controller (Elveflow OB1 MK3). The generated flow near the bottom wall was sufficiently approximated as a linear shear flow. The reference flow profiles were obtained from motions of fluorescent beads using a confocal microscope, where the total flow profile along the z axis was parabolic in this Hele-Shaw microchannel, and the local flow profile near the bottom wall showed linear shear flow. The shear rate near the wall was estimated from the flow speed 24.8 μm (the cell minor length) away from the wall. The flow profile on the xy plane was homogeneous and constant within the field of view.

Observation of ciliary beating of *T. pyriformis* in flow

To observe the ciliary beating of *T. pyriformis* in flow, we used a previously reported light sheet microscope, as shown in Fig. 2A (*5*, *27*). *T. pyriformis* was stained for 10 min in observation solution containing CellMask Orange plasma membrane stain (10 μg/ml; Molecular Probes) and washed three times with observation solution. The cells were introduced into a fluorinated ethylene polypropylene (FEP) tube (*28*) with a 1.2-mm inner diameter (JUNFRON, Junkosha), and one end of the tube was connected to a syringe with a pump (KDS 210, KD Scientific), which was used to apply the flow. After the chamber unit was filled with the observation solution, the tube was set so that the long axis of the tube coincided with the focus plane of the light sheet, which was generated by a line-scanning laser beam (FV10-LD559, Olympus) with a confocal laser scanning microscope (FV1000, Olympus). During the observation, the shear rate near the wall was maintained at $\dot{\gamma} = 5.0\ s^{-1}$.

Mathematical ciliate model for simulation

A swimmer model was developed in the same manner as that of Ohmura *et al.* (*5*). We derived a numerical method assuming $\mathbf{x} = (x, y, z)$ as an observation point and $\mathbf{y}$ as a source point. Assuming the surface traction acting on the cell surface $\mathbf{q}(\mathbf{y})$ and the thrust force per unit area $\mathbf{F}(\mathbf{x})$, the flow field is given by a boundary integral equation (*29*)

$$\mathbf{u}(\mathbf{x}) = \mathbf{u}_\infty(\mathbf{x}) - \int \mathbf{J_0}(\mathbf{x},\mathbf{y}) \cdot \mathbf{q}(\mathbf{y})\, dS_b(\mathbf{y}) - \int \mathbf{J_0}(\mathbf{x},\mathbf{y}) \cdot \mathbf{F}(\mathbf{y})\, dS_c(\mathbf{y}) \quad (1)$$

where dS_b and dS_c are the body surface and the stress surface, respectively. $\mathbf{J_0}(\mathbf{x},\mathbf{y}) = \frac{1}{8\pi\mu}\left(\frac{\delta_{ij}}{r} + \frac{r_i r_j}{r^3}\right)$ represents the single-layer potentials of Green's function, which is the second-order tensor called the Oseen tensor, where $\mathbf{r} = |\mathbf{r}|$ and $\mathbf{r} = \mathbf{x} - \mathbf{y}$. In addition, $\mathbf{u}_\infty(\mathbf{x})$ expresses the external flow field. In this calculation, $\mathbf{u}_\infty(\mathbf{x})$ is a shear flow.

Next, the flow field on the body surface, $\mathbf{u}_S(\mathbf{x})$, was determined using the velocity of the mass $\mathbf{U}$ and the turning angular velocity $\mathbf{\Omega}$ considering the nonslip boundary condition. The kinetic velocity on the body surface is described as follows

$$\mathbf{u}_S(\boldsymbol{x}) - \mathbf{u}_\infty(\boldsymbol{x}) = \mathbf{U} + \mathbf{\Omega} \wedge (\mathbf{x} - \mathbf{X_0}) \quad (2)$$

where $\mathbf{X_0}$ is the centroid of the swimmer body. Here, the external force $\mathbf{F}$ and torque $\mathbf{T}$ are taken as boundary conditions

$$\mathbf{F} = \int \mathbf{q}(\mathbf{y})\, dS_b(\mathbf{y}) = -\int \mathbf{F}(\mathbf{y})\, dS_c(\mathbf{y}) \quad (3)$$

$$\mathbf{T} = \int \mathbf{q}(\mathbf{y}) \wedge (\mathbf{y} - \mathbf{X_0})\, dS_b(\mathbf{y}) = -\int \mathbf{F}(\mathbf{y}) \wedge (\mathbf{y} - \mathbf{X_0}) dS_c(\mathbf{y}) \quad (4)$$

By solving the simultaneous Eqs. 1 to 4, $\mathbf{U}$, $\mathbf{\Omega}$, and $\mathbf{q}(\mathbf{x})$ can be derived. Once the translational and angular velocities were obtained, the material points were updated by a fourth-order Adams-Bashforth method.

Wall interactions introduced in the simulation

Assuming that a wall is a rigid and nonslip boundary, the swimmer experiences forces and torques from the wall. First, we consider the hydrodynamic interactions induced by the nonslip wall. The hydrodynamic interactions are derived using a modified Oseen tensor (*30*, *31*). The Oseen tensor $\mathbf{J_0}$ in the second term of Eq. 1 is changed to

$$\mathbf{J}(\mathbf{x},\mathbf{y}) = \mathbf{J_0}(\mathbf{x},\mathbf{y}) - \mathbf{J_w}(\mathbf{x},\mathbf{y}')$$

$$\mathbf{J_w}(\mathbf{x},\mathbf{y}') = -\mathbf{J_0}(\mathbf{x},\mathbf{y}') + 2h^2 \mathbf{J_D}(\mathbf{x},\mathbf{y}') - 2h\mathbf{J_{SD}}(\mathbf{x},\mathbf{y}')$$

where h is the distance between the center of the swimmer and the wall and $\mathbf{y}'$ is an imaginary source point of $\mathbf{y}$ at the opposite side of the wall

$$\mathbf{J_D}(\mathbf{x},\mathbf{y}') = \left(\frac{1 - 2\delta_{i3}}{8\pi\mu}\right)\left(\frac{\delta_{ij}}{r'^3} + \frac{3r'_i r'_j}{r'^5}\right)$$

$$\mathbf{J_{SD}}(\mathbf{x},\mathbf{y}') = \left(\frac{1 - 2\delta_{i3}}{8\pi\mu}\right)\left(\frac{\delta_{ij} r'_3 - \delta_{i3} r'_j + \delta_{j3} r'_i}{r'^3} - \frac{3r'_i r'_j r'_3}{r'^5}\right)$$

Next, we consider the repulsion from the rigid wall. When the swimmer approaches the wall, the swimmer sometimes collides with the wall. Therefore, the repulsion force and torque from the collision are added to Eqs. 3 and 4

$$\mathbf{F}_{rep} = \int \mathbf{F'}_{rep}(\mathbf{y})\, dS_a(\mathbf{y})$$

$$\mathbf{T}_{rep} = \int \mathbf{F'}_{rep}(\mathbf{y}) \wedge (\mathbf{y} - \mathbf{X_0})\, dS_a(\mathbf{y})$$

where $\mathbf{F'}_{rep}(\mathbf{y})$ is expressed as the repulsion force between the cilia and the wall per unit area. To reproduce the interaction between the cilia and the wall, we assume that the cilia are linear springs and $\mathbf{F'}_{rep}(\mathbf{y}) = kl_c(\mathbf{y})\mathbf{e_z}$, where $l_c(\mathbf{y})$ is the shrinking length of the cilia, k is the spring constant, and S_a is the area of cilia touching the wall. We do not consider friction with the wall in this calculation. Therefore, the repulsion force has only a z-axis component.

Last, we introduce an adaptive boundary condition of the cilia on the body surface. To reproduce the stopping of cilia beating near the wall, we define the SBA as depicted by the gray area on the bottom wall shown in Fig. 3B, where length a as the parameter of the SBA range corresponding to the length of cilia. The ciliary beating inside the SBA stops, and thus, the thrust force $\mathbf{F}(\mathbf{y})$ near the wall vanishes. When the ellipsoidal swimmer touches the bottom wall at a swimming angle of 11.9°, the ratio of the projected area of cilia stopping at $a = 0.3$ is 69.9%, which approximately corresponds to the value estimated by the experiment.

Shear flow applied in simulation

In this study, a shear flow is added as the external flow $\mathbf{u}_\infty$. The shear flow is applied to the whole system and dependent on the distance from the wall. The direction of the shear flow is along the x axis; therefore, the flow velocity $\mathbf{u}_\infty$ at $\mathbf{x} = (x, y, z)$ is defined as

$$\mathbf{u}_\infty = (u_\mathrm{f}, 0, 0), \quad \text{with} \quad u_\mathrm{f} = \dot{\gamma}_*(z - z_\mathrm{wall}) \tag{6}$$

where z_wall is the z coordinate of the wall and $z_\mathrm{wall} = -2$ in this calculation for internal simplicity. Taking this expression of $\boldsymbol{u}_\infty$ into Eq. 2, the arbitrary flow field is obtained.

Figure 3B shows a schematic figure of the numerical setup. The flow direction is along the x axis. At $z = -2$, the velocity is zero. The swimming angle on the xz plane is defined as θ_{xz}, and that on the xy plane is defined as θ_{xy}. The shape of the swimmer is spherical or prolate ellipsoidal (aspect ratio, 1:2). The diameter of the spherical swimmer is 2. The major length of the ellipsoidal swimmer is 2, and the minor length is 1. The minor length of the swimmer $L^* = 1.0$, and the speed of the swimmer without a wall $U^* = 1.0$. The time interval in the simulation $\mathrm{d}t = 0.01 \times L^*/U^* = 1$ step, which is 0.0881 s in real time. The shear rate in the simulation is γ_*, which is 11.3 s^{-1} in real units (see also table S1).

SUPPLEMENTARY MATERIALS

Supplementary material for this article is available athttps://science.org/doi/10.1126/sciadv.abi5878

View/request a protocol for this paper from *Bio-protocol*.

REFERENCES AND NOTES

1. T. Fenchel, The ecology of marine microbenthos II. The food of marine benthic ciliates. *Ophelia* **5**, 73–121 (1968).
2. T. Fenchel, The ecology of marine microbenthos IV. Structure and function of the benthic ecosystem, its chemical and physical factors and the microfauna commuities with special reference to the ciliated protozoa. *Ophelia* **6**, 1–182 (1969).
3. T. Fenchel, *The Ecology of Protozoa*. (Springer, 1987).
4. T. Fenchel, What can ecologists learn from microbes: Life beneath a square centimetre of sediment surface. *Funct. Ecol.* **6**, 499 (1992).
5. T. Ohmura, Y. Nishigami, A. Taniguchi, S. Nonaka, J. Manabe, T. Ishikawa, M. Ichikawa, Simple mechanosense and response of cilia motion reveal the intrinsic habits of ciliates. *Proc. Natl. Acad. Sci. U.S.A.* **115**, 3231–3236 (2018).
6. Y. Nishigami, T. Ohmura, A. Taniguchi, S. Nonaka, J. Manabe, T. Ishikawa, M. Ichikawa, Influence of cellular shape on sliding behavior of ciliates. *Commun. Integr. Biol.* **11**, e1506666 (2018).
7. G. P. Arnold, Rheotropism in fishes. *Biol. Rev. Camb. Philos. Soc.* **49**, 515–576 (1974).
8. J. C. Montgomery, C. F. Baker, A. G. Carton, The lateral line can mediate rheotaxis in fish. *Nature* **389**, 960–963 (1997).
9. P. Oteiza, I. Odstrcil, G. Lauder, R. Portugues, F. Engert, A novel mechanism for mechanosensory-based rheotaxis in larval zebrafish. *Nature* **547**, 445–448 (2017).
10. L. Ristroph, J. C. Liao, J. Zhang, Lateral line layout correlates with the differential hydrodynamic pressure on swimming fish. *Phys. Rev. Lett.* **114**, 018102 (2015).
11. V. Kantsler, J. Dunkel, M. Blayney, R. E. Goldstein, Correction: Rheotaxis facilitates upstream navigation of mammalian sperm cells. *eLife* **3**, e03521 (2014).
12. Marcos, H. C. Fu, T. R. Powers, R. Stocker, Bacterial rheotaxis. *Proc. Natl. Acad. Sci. U.S.A.* **109**, 4780–4785 (2012).
13. F. P. Bretherton, L. Rothschild, Rheotaxis of spermatozoa. *Proc. R. Soc. Lond. B. Biol. Sci.* **153**, 490–502 (1961).
14. M. Zaferani, S. H. Cheong, A. Abbaspourrad, Rheotaxis-based separation of sperm with progressive motility using a microfluidic corral system. *Proc. Natl. Acad. Sci. U.S.A.* **115**, 8272–8277 (2018).
15. A. J. T. M. Mathijssen, N. Figueroa-Morales, G. Junot, É. Clément, A. Lindner, A. Zöttl, Oscillatory surface rheotaxis of swimming *E. coli* bacteria. *Nat. Commun.* **10**, 3434 (2019).
16. T. Kaya, H. Koser, Direct upstream motility in Escherichia coli. *Biophys. J.* **102**, 1514–1523 (2012).
17. A. Bukatin, I. Kukhtevich, N. Stoop, J. Dunkel, V. Kantsler, Bimodal rheotactic behavior reflects flagellar beat asymmetry in human sperm cells. *Proc. Natl. Acad. Sci. U.S.A.* **112**, 15904–15909 (2015).
18. J. Yuan, D. M. Raizen, H. H. Bau, Propensity of undulatory swimmers, such as worms, to go against the flow. *Proc. Natl. Acad. Sci. U.S.A.* **112**, 3606–3611 (2015).
19. T. Omori, T. Ishikawa, Upward swimming of a sperm cell in shear flow. *Phys. Rev. E* **93**, 32402 (2016).
20. K. Ishimoto, E. A. Gaffney, Fluid flow and sperm guidance: A simulation study of hydrodynamic sperm rheotaxis. *J. R. Soc. Interface* **12**, 20150172 (2015).
21. K. Ishimoto, Guidance of microswimmers by wall and flow: Thigmotaxis and rheotaxis of unsteady squirmers in two and three dimensions. *Phys. Rev. E* **96**, 043103 (2017).
22. H. S. Jennings, The behavior of paramecium. Additional features and general relations. *J. Comp. Neurol. Psychol.* **XIV**, 441–510 (1904).
23. G. Jing, A. Zöttl, É. Clément, A. Lindner, Chirality-induced bacterial rheotaxis in bulk shear flows. *Sci. Adv.* **6**, eabb2012 (2020).
24. K. Ishimoto, Helicoidal particles and swimmers in a flow at low Reynolds number. *J. Fluid Mech.* **892**, A11 (2020).
25. S. L. Tamm, Ciliary motion in *PARAMECIUM*: A scanning electron microscope study. *J. Cell Biol.* **55**, 250–255 (1972).
26. Y. Muto, Y. Tanabe, K. Kawai, Y. Okano, H. Iio, Climacostol inhibits *Tetrahymena* motility and mitochondrial respiration. *Cent. Eur. J. Biol.* **6**, 99–104 (2011).
27. D. Takao, A. Taniguchi, T. Takeda, S. Sonobe, S. Nonaka, High-speed imaging of amoeboid movements using light-sheet microscopy. *PLOS ONE* **7**, e50846 (2012).
28. A. Kaufmann, M. Mickoleit, M. Weber, J. Huisken, Multilayer mounting enables long-term imaging of zebrafish development in a light sheet microscope. *Development* **139**, 3242–3247 (2012).
29. F. Rizzo, *Boundary Integral and Singularity Methods for Linearized Viscous Flow (C. Pozrikidis)*. (SIAM Review, Cambridge Univ. Press, 1994), vol. 36.
30. J. R. Blake, A note on the image system for a stokeslet in a no-slip boundary. *Math. Proc. Camb. Philos. Soc.* **70**, 303–310 (1971).
31. J. Manabe, T. Omori, T. Ishikawa, Shape matters: Entrapment of a model ciliate at interfaces. *J. Fluid Mech.* **892**, A15 (2020).
32. G. Barker Jeffery, The motion of ellipsoidal particles immersed in a viscous fluid. *Proc. R. Soc. Lond. A* **102**, 161–179 (1922).

Acknowledgments

Funding: This work was performed under the Cooperative Research Program of the "Network Joint Research Center for Materials and Devices" (to Y.N. and M.I.) and the Program for Fostering Researchers for the Next Generation conducted by the Consortium Office for the Fostering of Researchers in Future Generations, Hokkaido University (to Y.N.). This work was supported by JSPS KAKENHI grant nos. 19KK0180 (to Y.N.), 17J10331 (to T.O.), 17H00853 (to T.I.), 21H04999 (to T.I.), 26707020 (to M.I.), and 21K03855 (to M.I.), the JSPS Core-to-Core Program, A. Advanced Research Networks (to Y.N.), a research grant from the Kurita Water and Environment Foundation (grant no. 20E028) (to Y.N.), the NIBB Collaborative Research Program to 20-501 (to Y.N.), and the Human Frontier Science Program LT000013/2019-C (to T.O.) **Author contributions:** T.O., Y.N., and M.I. designed the work and analyzed and interpreted the experimental and simulation data. T.O. and Y.N. performed the experiment. A.T. and S.N. developed the experimental setup. T.O. performed the simulation. T.I. developed the simulation model. T.O., Y.N., and M.I. drafted the work. **Competing interests:** The authors declare that they have no competing interests. **Data and materials availability:** All data needed to evaluate the conclusions in the paper are present in the paper and/or the Supplementary Materials.

Submitted 22 March 2021
Accepted 25 August 2021
Published 20 October 2021
10.1126/sciadv.abi5878

Citation: T. Ohmura, Y. Nishigami, A. Taniguchi, S. Nonaka, T. Ishikawa, M. Ichikawa, Near-wall rheotaxis of the ciliate *Tetrahymena* induced by the kinesthetic sensing of cilia. *Sci. Adv.* **7**, eabi5878 (2021).

ScienceAdvances

Near-wall rheotaxis of the ciliate *Tetrahymena* induced by the kinesthetic sensing of cilia

Takuya OhmuraYukinori NishigamiAtsushi TaniguchiShigenori NonakaTakuji IshikawaMasatoshi Ichikawa

Sci. Adv., 7 (43), eabi5878. • DOI: 10.1126/sciadv.abi5878